Blind Restoration of Poisson Images Using Adaptive Euler's Elastica Regularization

Hanwen Cao, Jun Zhang, Sanping Rao, Chao Yi, Mengling He

***Abstract*—In a wide range of applications such as astronomy, biology, and medical imaging, acquired data are often corrupted by Poisson noise and blurring artifacts. Poisson noise is difficult to eliminate due to its signal-dependent and multiplicative properties. In this paper, a new adaptive Euler's elastica regularization model for blind restoration of Poisson images is proposed. This model combines the advantages of an adaptive weighted matrix and Euler's elastica regularization, which can mitigate the staircase effects while effectively preserving the local features of the image. In addition, an efficient alternating direction method of multipliers (ADMM) for solving this nonconvex model is designed. A large number of experiments are carried out on natural and synthetic images, respectively. The related results show that the proposed method can not only obtain a more accurate blur kernel but also improve the quality of the recovered image significantly.**

***Index Terms*—Blind restoration, Poisson noise, Euler's elastica regularization, Adaptive weighted matrix, ADMM**

I. Introduction

DATA captured by the imaging sensor faces various forms of degradation, with noise and blurring being the most significant. Recent progress in fluorescence microscopy [1], [2], positron emission tomography [3], and single photon emission computed tomography [4] has highlighted the importance of studying Poisson noise in images. Poisson distribution is a better fit for describing noise statistics in photon counting systems compared to the conventional Gaussian distribution. Poisson noise differs from Gaussian noise as it is neither purely additive nor multiplicative. It is a signal-dependent noise that varies with the pixel intensity peak. This makes restoring images affected by Poisson noise particularly challenging. Mathematically, the model for image degradation caused by Poisson noise is usually expressed as

$$f = \mathcal{P}(Ku), \tag{1}$$

Manuscript received May 13, 2024; revised September 1, 2024.

This work was partly supported by the Jiangxi Provincial Natural Science Foundation (20232BAB201017, 20242BAB22013), the National Natural Science Foundation of China (62461043), and the Jiangxi Provincial University Humanities and Social Sciences Research Project (TJ23101).

Hanwen Cao is an associate professor at the College of Science, and the Key Laboratory of Engineering Mathematics and Advanced Computing, Nanchang Institute of Technology, Nanchang 330099, Jiangxi, China. (e-mail: hanwencao21@163.com).

Jun Zhang is an associate professor at the College of Science, Nanchang Institute of Technology, Nanchang 330099, Jiangxi, China. (corresponding author, e-mail: junzhang0805@126.com).

Sanping Rao is an associate professor at the College of Science, Nanchang Institute of Technology, Nanchang 330099, Jiangxi, China. (e-mail: raosanping81@sina.com).

Chao Yi is a postgraduate student at the College of Science, Nanchang Institute of Technology, Nanchang 330099, Jiangxi, China. (e-mail: chaoyi1002@126.com).

Mengling He is a postgraduate student at the College of Science, Nanchang Institute of Technology, Nanchang 330099, Jiangxi, China. (e-mail: heml0816@163.com).

where f and u represent the degraded image and the original clear image, respectively, and K denotes the convolution matrix form of the point spread function (PSF), also referred to as the blur kernel. The Poisson function captures the process of Poisson noise degradation.

The inverse process of blurring is often called deconvolution, which seeks to find the best estimates of K and u from the degraded image f. The problem of deconvolution can be classified into two types based on whether prior knowledge of the PSF is available or not: non-blind deconvolution and blind deconvolution. Numerous non-blind deconvolution methods using regularization have been developed over time, such as TV regularization [5], [6], higher-order TV regularization [7], fractional-order TV [8], total generalized variation regularization [9], and curvature-based regularization [10], [11].

In contrast to non-blind deconvolution, blind deconvolution is more complex due to the lack of prior knowledge about the blur kernel, compounded by the nonlinear and non-quadratic characteristics of the Poisson distribution. Early research in this field focused on Expectation Maximization (EM) algorithms. For instance, a method using the RL algorithm, which is a specific form of the EM approach, has been proposed in [12]. In this method, the PSF is initially kept constant while RL iterations update the latent image, and then the latent image is held steady while RL iterations adjust the PSF. These two steps are repeated alternately until a final result is achieved. In [13], the authors proposed regularizing the latent image using a Huber-Markov random field and implemented an alternating algorithm similar to that described in [12] for iterative optimization of the latent image and the PSF. The authors enhanced the traditional alternation method in two ways, as described in [14] and [15]. First, they introduced more efficient sparse-constrained regularization by performing wavelet or small frame decomposition of the latent image. Second, they employed the split Bregman method [16] or the ADMM algorithm [17] to structure the EM approach for estimating the latent image. Nonetheless, the PSF continued to use a one-step delay scheme for updating. In [18], the authors combined an l_0 sparse prior with TV regularization in blind deconvolution to recover the latent image using a greedy analytic tracking algorithm. This approach integrates the EM method for internal iterations, with the PSF being similarly estimated using a delayed one-step process. In [19], the authors proposed using FOTV regularization to address both blur and Poisson noise, still employing EM algorithm. However, these EM-based alternating optimization methods may lead to unsatisfactory results when the energy distribution of the PSFs is complex, such as in cases of PSFs induced by motion.

In [20], the authors used the l_0 norm and TV of the image gradient to regularize the latent image and PSF, respectively.

They proposed a method that combines variable splitting and Lagrange multipliers. Initially, the PSF is estimated using an enhanced IPLS algorithm, followed by employing a variable splitting method that includes an image smoothing operator for image restoration. Additionally, with advances in machine learning, deep learning has emerged as an effective tool for blind restoration of Poisson images [21]. While deep learning methods generally require substantial training data, obtaining sufficient data in real-world blurring situations can be challenging. Moreover, due to the unique nature of blurred image restoration across different scenarios, the application of deep learning is somewhat constrained.

In recent years, Euler's elastica regularization has demonstrated effectiveness in various applications, such as color image restoration [22], image segmentation [23], and 3D surface reconstruction [24], [25]. This approach has also been applied to Poisson image deconvolution [26]. The authors have introduced a Poisson image restoration model using adaptive Euler's elastica regularization, which mitigates the staircase effects often associated with the TV model due to its higher-order nature. This model effectively preserves image features and structural details in smoothed regions.

Recently, Pang et al. [6], [27] introduced regularization methods that use an adaptive weighted matrix combined with a gradient operator for image denoising. The adaptive weighted matrix adjusts the orientation of the gradient operator to favor higher weights, thereby more effectively capturing the local features of the image. Building on our recent research, in which we proposed a Gaussian image blind restoration model based on adaptive Euler's elastica regularization and achieved improved restoration results [28], we are inspired to develop a new adaptive Euler's elastica Poisson image blind restoration model. Furthermore, instead of employing the traditional EM-based alternating optimization algorithm, we design a more robust optimization method known as the alternating direction method of multipliers (ADMM). This approach transforms the original Poisson image blind restoration problem into the alternating computation of several subproblems. The key contributions of this paper can be summarized as follows:

Models based on Euler's elastica regularization are not often applied to the blind restoration of Poisson images. We introduce a novel adaptive Euler's elastica regularization model for blind deconvolution of Poisson images. By incorporating an adaptive weighting matrix into the Euler's elastica regularization, the model becomes more adaptable and robust. This approach allows for more effective mitigation of the staircase effects and helps preserve image details.

Numerous experiments on both natural and synthetic images are conducted to demonstrate the effectiveness of the proposed model and algorithm. In the context of Poisson image blind restoration, we compare our model against the EM model and the FOTV model.

II. Proposed model

Although the TV model is effective in maintaining sharp edges in an image, it can often lead to unwanted staircase effects in regions of uniform intensity. To address this issue, higher-order models like curvature regularization have been proposed. Drawing inspiration from the successful application of curvature regularization, we introduce a new Poisson blind restoration model as follows:

$$\begin{aligned}\min_{u,k}\sum_{i,j} g_1(\kappa(u_{i,j}))|\mathbf{T}\nabla u_{i,j}| + \beta\|\nabla k\|_1 \\ + \lambda\int_\Omega (Ku - f\log Ku)\mathrm{d}\mathbf{x}.\end{aligned} \tag{2}$$

Here,

$$g_1(\kappa(u_{i,j})) = 1 + \alpha \mid \kappa(u_{i,j}) \mid, \tag{3}$$

where $\alpha > 0$ is a constant. In a two-dimensional curve, the curvature κ can be expressed as a function of u, i.e.

$$\kappa(u_{i,j}) = \nabla\cdot\left(\frac{\nabla u_{i,j}}{|\nabla u_{i,j}|}\right). \tag{4}$$

The adaptive weighted matrix $\mathbf{T}$ is defined as follows:

$$\begin{aligned}\mathbf{T}(i,j) &= \begin{bmatrix} t_1(i,j) & 0 \\ 0 & t_2(i,j)\end{bmatrix} \\ &= \begin{bmatrix} \frac{1}{1+\iota|G_\delta(i,j)*\nabla_x f(i,j)|} & 0 \\ 0 & \frac{1}{1+\iota|G_\delta(i,j)*\nabla_y f(i,j)|}\end{bmatrix},\end{aligned} \tag{5}$$

where $\mathbf{G}_\delta(\cdot)$ stands for a two-dimensional Gaussian convolution kernel, ι and δ are two tuning parameters. $\nabla_x f$ and $\nabla_y f$ signify the differences in the horizontal and vertical directions, respectively.

By incorporating an adaptive weighted matrix into the Euler's elastica regularization, the model adapts more effectively to various image structures, resulting in superior performance in recovering smooth images.

III. Numerical solution

The direct solution of the nonconvex and nonsmooth minimization problem (2) is exceedingly difficult due to its inherent complexity. To address this issue, we develop an efficient alternating direction method of multipliers (ADMM) that simplifies the resolution of the original problem by iteratively solving a series of interconnected subproblems in an alternating fashion.

We first introduce four auxiliary variables $\mathbf{p}$, $\mathbf{q}$, $\mathbf{w}$ and g to transform the original unconstrained problem (2) into the following constrained optimization problem:

$$\begin{aligned}\min_{u,k,\mathbf{p},\mathbf{q},\mathbf{w},g}\sum_{i,j} g_1\left(\kappa\left(u_{i,j}\right)\right)|\mathbf{q}_{i,j}| + \beta\|\mathbf{w}\|_1 \\ + \lambda\int_\Omega (g - f\log g)\,\mathrm{d}\mathbf{x}, \\ \text{s.t.}\quad \mathbf{p} = \nabla u, \mathbf{q} = \mathbf{T}\mathbf{p}, \mathbf{w} = \nabla k, g = Ku.\end{aligned} \tag{6}$$

To solve (6), four Lagrangian multipliers $\boldsymbol{\lambda}_i = (\lambda_{i1}, \lambda_{i2})^T$, $i = 1, 2, 3$, and λ_4 are introduced. Then we reformulate it as a saddle point problem. The corresponding augmented Lagrangian functional is

$$\begin{aligned}&\mathcal{L}(k, u, \mathbf{p}, \mathbf{q}, \mathbf{w}, g; \boldsymbol{\lambda}_1, \boldsymbol{\lambda}_2, \boldsymbol{\lambda}_3, \lambda_4) \\ =&\sum_{i,j} g_1\left(\kappa\left(u^n_{i,j}\right)\right)|\mathbf{q}_{i,j}| + \beta\|\mathbf{w}\|_1 + \lambda\int_\Omega (g - f\log g)\mathrm{d}\mathbf{x} \\ &+ \frac{r_1}{2}\|\mathbf{p} - \nabla u - \boldsymbol{\lambda}_1\|_2^2 + \frac{r_2}{2}\|\mathbf{q} - \mathbf{T}\mathbf{p} - \boldsymbol{\lambda}_2\|_2^2 \\ &+ \frac{r_3}{2}\|\mathbf{w} - \nabla k - \boldsymbol{\lambda}_3\|_2^2 + \frac{r_4}{2}\|g - Ku - \lambda_4\|_2^2,\end{aligned} \tag{7}$$

where $r_1, r_2, r_3, r_4 > 0$ are penalty parameters. Given the complexity of equation (6), which involves six subvariables, we employ the ADMM to tackle each subvariable alternately and iteratively. This approach ensures that each subvariable is addressed in a systematic and efficient manner, facilitating the overall solution process. Please refer to Algorithm 1 for details.

Algorithm 1 ADMM for solving (2)

1. Input: a blurred and noisy image f;
2. Parameters: λ, ι, δ, β, α, nMax and $\epsilon \in \mathbb{R}$;
3. Initialization: $u^0 = f$, $n = 0$, and $\mathbf{p}^0 = \boldsymbol{\lambda}_1^0 = \mathbf{q}^0 = \boldsymbol{\lambda}_2^0 = \mathbf{w}^0 = \boldsymbol{\lambda}_3^0 = \mathbf{0}$, $g = \lambda_4^0 = 0$;
4.While $n <$nMax do (8)
5. Replace n with $n + 1$;
6. If $\| u^n - u^{n-1} \|_F / \| u^n \|_F \leq \epsilon$, stop the iteration;
7. End while;
8. Return $u^* = u^n$ as the final recovered image and $k^* = k^n$ as the final recovered blur kernel.

The efficiency of Algorithm 1 for solving the optimization problem (2) hinges on its ability to efficiently resolve the subproblems.

- The k-subproblem can be reformulated as

$$\begin{aligned} k^{n+1} = \arg\min_k \frac{r_3}{2} \left\| \mathbf{w}^n - \nabla k - \boldsymbol{\lambda}_3^n \right\|_2^2 \\ + \frac{r_4}{2} \left\| g^n - K u^n - \lambda_4^n \right\|_2^2 . \end{aligned} \tag{9}$$

Under periodic boundary conditions, the Euler-Lagrange equation of this subproblem can be solved efficiently by fast Fourier transform (FFT). It follows that

$$\begin{aligned} & k^{n+1} \\ =& F^{-1}\left[\frac{F\left(r_4 (U^n)^T (\lambda_4^n - g^n) - r_3 \operatorname{div}(\boldsymbol{\lambda}_3^n - \mathbf{w}^n)\right)}{F\left(r_3 \Delta - r_4 (U^n)^T U^n\right)}\right], \end{aligned} \tag{10}$$

where F and F^{-1} denote the FFT and its inverse transform, respectively, and Δ is the Laplace operator.

- The u-subproblem can be written as

$$\begin{aligned} u^{n+1} = \arg\min_u \frac{r_1}{2} \| \mathbf{p}^n - \nabla u - \boldsymbol{\lambda}_1^n \|_2^2 \\ + \frac{r_4}{2} \left\| g^n - K^{n+1} u - \lambda_4^n \right\|_2^2 . \end{aligned} \tag{11}$$

Using the FFT again, we have

$$\begin{aligned} & u^{n+1} \\ =& F^{-1}\left[\frac{F\left(r_4 (K^{n+1})^T (\lambda_4^n - g^n) - r_1 \operatorname{div}(\boldsymbol{\lambda}_1^n - \mathbf{p}^n)\right)}{F\left(r_1 \Delta - r_4 (K^{n+1})^T K^{n+1}\right)}\right]. \end{aligned} \tag{12}$$

- The $\mathbf{p}$-subproblem can be expressed as

$$\begin{aligned} \mathbf{p}^{n+1} = \arg\min_{\mathbf{p}} \frac{r_1}{2} \left\| \mathbf{p} - \nabla u^{n+1} - \boldsymbol{\lambda}_1^n \right\|_2^2 \\ + \frac{r_2}{2} \| \mathbf{q}^n - \mathbf{T}\mathbf{p} - \boldsymbol{\lambda}_2^n \|_2^2 . \end{aligned} \tag{13}$$

Based on its optimality condition, the corresponding system of linear equations can be derived as

$$\begin{aligned} & \begin{bmatrix} r_1 + r_2 t_1^2 & 0 \\ 0 & r_1 + r_2 t_2^2 \end{bmatrix} \begin{bmatrix} p_1^{n+1} \\ p_2^{n+1} \end{bmatrix} \\ =& \begin{bmatrix} r_1 \left(\nabla_x u^{n+1} + \lambda_{11}^n\right) + r_2 t_1 \left(q_1^n - \lambda_{21}^n\right) \\ r_1 \left(\nabla_y u^{n+1} + \lambda_{12}^n\right) + r_2 t_2 \left(q_2^n - \lambda_{22}^n\right) \end{bmatrix}. \end{aligned} \tag{14}$$

From this equation, an explicit solution for $\mathbf{p}^{n+1}$ can be obtained, namely

$$\begin{cases} p_1^{n+1} = \dfrac{r_1 \left(\nabla_x u^{n+1} + \lambda_{11}^n\right) + r_2 t_1 \left(q_1^n - \lambda_{21}^n\right)}{r_1 + r_2 t_1^2}, \\ p_2^{n+1} = \dfrac{r_1 \left(\nabla_y u^{n+1} + \lambda_{12}^n\right) + r_2 t_2 \left(q_2^n - \lambda_{22}^n\right)}{r_1 + r_2 t_2^2}. \end{cases} \tag{15}$$

- The $\mathbf{q}$-subproblem can be expressed as

$$\begin{aligned} \mathbf{q}^{n+1} = \arg\min_{\mathbf{q}} \sum_{i,j} g_1\left(\kappa(u_{i,j}^n)\right) |\mathbf{q}_{i,j}| \\ + \frac{r_2}{2} \left\| \mathbf{q} - \mathbf{T}\mathbf{p}^{n+1} - \boldsymbol{\lambda}_2^n \right\|_2^2 . \end{aligned} \tag{16}$$

Its closed-form solution can then be computed by the soft-threshold operator as follows:

$$\begin{aligned} \mathbf{q}_{i,j}^{n+1} &= \operatorname{soft}\left((\mathbf{T}\mathbf{p}^{n+1} + \boldsymbol{\lambda}_2^n)_{i,j}, \frac{g_1\left(\kappa(u_{i,j}^n)\right)}{r_2} \right) \\ &= \max\left(\left| \left(\mathbf{T}\mathbf{p}^{n+1} + \boldsymbol{\lambda}_2^n\right)_{i,j} \right| - \frac{g_1\left(\kappa(u_{i,j}^n)\right)}{r_2}, 0 \right) \\ &\quad \cdot \operatorname{sign}\left((\mathbf{T}\mathbf{p}^{n+1} + \boldsymbol{\lambda}_2^n)_{i,j} \right). \end{aligned} \tag{17}$$

- The $\mathbf{w}$-subproblem is as follows:

$$\mathbf{w}^{n+1} = \arg\min_{\mathbf{w}} \beta \|\mathbf{w}\|_1 + \frac{r_3}{2} \|\mathbf{w} - \nabla k^{n+1} - \boldsymbol{\lambda}_3^n\|_2^2. \tag{18}$$

Similarly, the solution of this subproblem can be given by the soft-threshold operator, namely

$$\mathbf{w}_{i,j}^{n+1} = \operatorname{soft}\left((\nabla k^{n+1} + \boldsymbol{\lambda}_3^n)_{i,j}, \frac{\boldsymbol{\beta}}{\boldsymbol{r}_3} \right). \tag{19}$$

- The g-subproblem can be written as

$$\begin{aligned} g^{n+1} = \arg\min_g \lambda \int_\Omega (g - f \log g) \mathrm{d}\mathbf{x} \\ + \frac{r_4}{2} \left\| g - K^{n+1} u^{n+1} - \lambda_4^n \right\|_2^2 . \end{aligned} \tag{20}$$

By solving the quadratic equation, its solution can be obtained,

$$\begin{aligned} g^{n+1} = & \frac{K^{n+1} u^{n+1} + \lambda_4^n - \frac{\lambda}{r_4}}{2} \\ & + \sqrt{\left(\frac{K^{n+1} u^{n+1} + \lambda_4^n - \frac{\lambda}{r_4}}{2} \right)^2 + \frac{\lambda f}{r_4}}. \end{aligned} \tag{21}$$

Note that the solution (u, k) produced by the proposed model may not be unique. To achieve a unique and reasonable solution, specific constraints need to be applied to u and k. During the iteration process, we apply a sum of one and non-negative constraints, similar to the blind restoration of Gaussian images in [28]. These constraints help maintain convergence. That is, we set

$$\int k^n(x, y) \mathrm{d}\mathbf{x} = 1, \tag{22}$$

$$u^n(x, y) = \begin{cases} u^n(x, y), & u^n(x, y) \geq 0, \\ 0, & \text{else.} \end{cases} \tag{23}$$

Additionally, we use dynamic threshold constraints to enhance the PSF, namely

$$k^n(x, y) = \begin{cases} k^n(x, y), & k^n(x, y) \geq \xi \max(k^n), \\ 0, & \text{else,} \end{cases} \tag{24}$$

$$\begin{cases} k^{n+1} = \arg\min\limits_{k} \mathcal{L}\left(k, u^n, \mathbf{p}^n, \mathbf{q}^n, \mathbf{w}^n, g^n; \boldsymbol{\lambda}_1^n, \boldsymbol{\lambda}_2^n, \boldsymbol{\lambda}_3^n, \lambda_4^n\right), \\ u^{n+1} = \arg\min\limits_{u} \mathcal{L}\left(k^{n+1}, u, \mathbf{p}^n, \mathbf{q}^n, \mathbf{w}^n, g^n; \boldsymbol{\lambda}_1^n, \boldsymbol{\lambda}_2^n, \boldsymbol{\lambda}_3^n, \lambda_4^n\right), \\ \mathbf{p}^{n+1} = \arg\min\limits_{\mathbf{p}} \mathcal{L}\left(k^{n+1}, u^{n+1}, \mathbf{p}, \mathbf{q}^n, \mathbf{w}^n, g^n; \boldsymbol{\lambda}_1^n, \boldsymbol{\lambda}_2^n, \boldsymbol{\lambda}_3^n, \lambda_4^n\right), \\ \mathbf{q}^{n+1} = \arg\min\limits_{\mathbf{q}} \mathcal{L}\left(k^{n+1}, u^{n+1}, \mathbf{p}^{n+1}, \mathbf{q}, \mathbf{w}^n, g^n; \boldsymbol{\lambda}_1^n, \boldsymbol{\lambda}_2^n, \boldsymbol{\lambda}_3^n, \lambda_4^n\right), \\ \mathbf{w}^{n+1} = \arg\min\limits_{\mathbf{w}} \mathcal{L}\left(k^{n+1}, u^{n+1}, \mathbf{p}^{n+1}, \mathbf{q}^{n+1}, \mathbf{w}, g^n; \boldsymbol{\lambda}_1^n, \boldsymbol{\lambda}_2^n, \boldsymbol{\lambda}_3^n, \lambda_4^n\right), \\ g^{n+1} = \arg\min\limits_{g} \mathcal{L}\left(k^{n+1}, u^{n+1}, \mathbf{p}^{n+1}, \mathbf{q}^{n+1}, \mathbf{w}^{n+1}, g; \boldsymbol{\lambda}_1^n, \boldsymbol{\lambda}_2^n, \boldsymbol{\lambda}_3^n, \lambda_4^n\right), \\ \boldsymbol{\lambda}_1^{n+1} = \boldsymbol{\lambda}_1^n + \nabla u^{n+1} - \mathbf{p}^{n+1}, \quad \boldsymbol{\lambda}_2^{n+1} = \boldsymbol{\lambda}_2^n + \mathbf{T}\mathbf{p}^{n+1} - \mathbf{q}^{n+1}, \\ \boldsymbol{\lambda}_3^{n+1} = \boldsymbol{\lambda}_3^n + \nabla k^{n+1} - \mathbf{w}^{n+1}, \quad \lambda_4^{n+1} = \lambda_4^n + K^{n+1}u^{n+1} - g^{n+1}. \end{cases} \tag{8}$$

where we denote $\max(k^n)$ as the maximum value of the nth estimated PSF. ξ is a small positive constant, which is set to 0.05 in our experiments.

IV. Experimental results and analysis

We carry out extensive experiments on both natural and synthetic images, comparing the numerical results and visual outcomes with those obtained using the FOTV model [29] and the EM model [30], in order to show the effectiveness and superiority of our proposed method. For ease of description, we refer to our proposed method as AEEPBD.

All numerical experiments were performed in the MATLAB environment on a PC equipped with a 2.50 GHz Intel(R) Core(TM) i5-12500 CPU and 16 GB RAM. We use peak-signal-to-noise ratio (PSNR), improved signal-to-noise ratio (ISNR), and structural similarity (SSIM) as quantitative metrics to assess the quality of the recovered images. Specifically, the PSNR used in experiments is defined as

$$\mathrm{PSNR} = 10\log_{10}\frac{P^2}{\frac{1}{MN}\sum\limits_{i=1}^{M}\sum\limits_{j=1}^{N}\left(u_{i,j} - I_{i,j}\right)^2}, \tag{25}$$

where P signifies the image peak, $I_{i,j}$ and $u_{i,j}$ respectively denote the pixel values of the clean and recovered images. N and M represent the width and length of the image, respectively. In the simulation experiments, we choose $P = 255$, 1000, and 3000, each peak representing a specific Poisson noise level. A smaller peak value makes the image appear noisier, thus increasing the difficulty of recovery. The definition of ISNR is as follows:

$$\mathrm{ISNR} = 10\log_{10}\frac{\|f - I\|_F^2}{\|u - I\|_F^2}, \tag{26}$$

where f stands for the degraded image. And SSIM is defined by

$$\mathrm{SSIM} = \frac{(2\mu_I\mu_u + c_1)(2\sigma_{Iu} + c_2)}{({\mu_I}^2 + {\mu_u}^2 + c_1)({\sigma_I}^2 + {\sigma_u}^2 + c_2)}, \tag{27}$$

where μ_I and μ_u denote the mean values of the images I and u, respectively. σ_I and σ_u signify their standard deviations. σ_{Iu} represents the covariance between I and u. c_1 and c_2 are two positive constants that prevent a zero denominator from occurring. The relative error is calculated by

$$R(u^n) = \frac{\|u^n - u^{n-1}\|_F}{\|u^n\|_F}. \tag{28}$$

In our experiments, the iteration will be terminated when the relative error $R(u^n) \le 10^{-4}$ or iteration reaches 500 steps.

Four test images are chosen in experiments, including natural images ("Satellite" (128×128), "Spine" (490×367)) and synthetic images ("Brain" (210×210), "Triangle" (254×214)), as shown in Fig. 1.

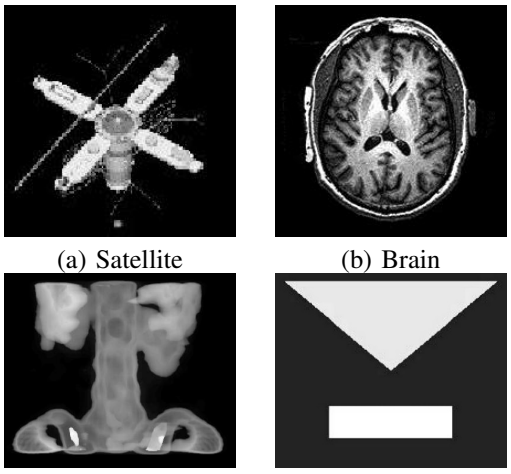

(a) Satellite (b) Brain (c) Spine (d) Triangle

Fig. 1. Test images.

We use the "fspecial" command in MATLAB to add different types of blur kernels to the image. Specifically, we utilize Gaussian blur (fspecial('gaussian', 7, 10)) and motion blur (fspecial('motion', 11, 45)), as demonstrated in Fig. 2.

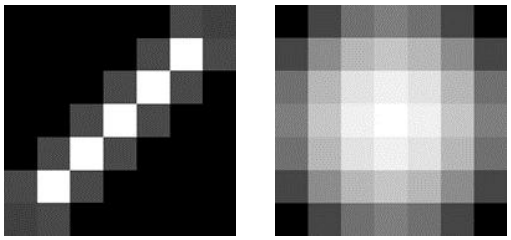

(a) linear motion (b) Gaussian

Fig. 2. Blur kernels for image degradation.

For Poisson image blind restoration, multiple parameters in the proposed AEEPBD need to be adjusted to achieve the optimal restoration effect. Specifically, a trial-and-error approach is employed for the gradual adjustment of parameters. The specific steps are as follows. We begin with initial estimates for the model and algorithm parameters based on

experience. Then we adjust each parameter incrementally within a reasonable range and test the model's performance using PSNR. Further, based on the performance evaluation, we tune the parameters that seem to have the most significant impact on the restoration quality. Finally, we repeat the above two steps until the optimal set of parameters that maximizes the quality of the restored image is found. The parameters included in the other two comparison methods are adjusted using the same strategy described above.

During the parameter tuning process, we found that λ, β, α, ι, δ have a significant influence on the results. λ is used to control the balance between the fidelity term and the regularization term, and we set $\lambda \in [2 \times 10^2, 2.5 \times 10^3]$. β is a regularization parameter about the blur kernel, which affects the diffusion of the PSF. In the experiments, we select $\beta \in [1 \times 10^2, 2 \times 10^3]$. Additionally, α is used to balance the curvature term and the length, and its value should be chosen reasonably in order to retain more image details. And its value is selected as $\alpha \in [1 \times 10^{-2}, 1.5]$. The parameters ι and δ are from the adaptive weighted matrix. ι is a tuning parameter used to control the local adaptivity and δ means the standard deviation. Their values can be referred to [31]. r_1, r_2, r_3, r_4 are four penalty parameters that affect the convergence speed and stability of the proposed algorithm. We choose $r_1 \in [1 \times 10^{-3}, 2.5], r_2 \in [1 \times 10^{-2}, 4], r_3 \in [1 \times 10^{-4}, 12]$. During the parameter tuning process, we usually set the value of r_4 to a multiple of 5. Tables I-IV list the corresponding numerical results of the three approaches on four test images, respectively. These results show that the AEEPBD has better performance in Poisson image blind restoration.

TABLE I Numerical results obtained using different models for "Satellite" images under different types of blur and noise levels.

Blur	P	Model	PSNR	ISNR	SSIM
Motion	3000	EM	25.22	5.37	0.900
		FOTV	25.63	5.78	0.902
		AEEPBD	**25.95**	**6.10**	**0.904**
	1000	EM	24.16	4.35	0.895
		FOTV	24.62	4.81	**0.900**
		AEEPBD	**24.84**	**5.03**	**0.900**
	255	EM	22.89	3.21	0.919
		FOTV	23.20	3.52	0.924
		AEEPBD	**23.40**	**3.72**	**0.926**
Gaussian	3000	EM	24.57	3.38	0.853
		FOTV	25.15	3.96	0.863
		AEEPBD	**25.36**	**4.17**	**0.875**
	1000	EM	23.15	3.52	0.859
		FOTV	24.03	4.40	0.867
		AEEPBD	**24.21**	**4.58**	**0.871**
	255	EM	20.37	3.15	0.860
		FOTV	21.28	4.06	0.867
		AEEPBD	**21.45**	**4.32**	**0.870**

Note: Bold indicates the optimal value for each index.

To evaluate the quality of the images recovered through different methods, visual images are provided for each test image, including the recovered image, the recovered blur kernel, the locally enlarged image, and the residual image (see Figs. 3-6). From these figures, we observe that when the added blur is the same, the performance of each method diminishes as the peak value decreases. This decline occurs because, regardless of the robustness of the algorithm, high-level noise in blurry images often leads to low-quality outcomes in blind image restoration. Nevertheless, AEEPBD consistently achieves the most favorable recovery results, particularly at high noise levels. In Fig. 3, it can be seen that AEEPBD outperforms the FOTV and EM models in eliminating noise and blur, resulting in clearer restoration results. Specifically, we observe from the body part of the "Satellite" image that the restoration result of the EM model is excessively blurred, leading to the loss of many details,

TABLE II Numerical results acquired by different models for "Spine" images under different types of blur and noise levels.

Blur	P	Model	PSNR	ISNR	SSIM
Motion	3000	EM	35.07	6.93	0.970
		FOTV	35.45	7.31	0.977
		AEEPBD	**35.67**	**7.53**	**0.983**
	1000	EM	33.70	6.45	0.954
		FOTV	34.15	6.90	0.960
		AEEPBD	**34.36**	**7.11**	**0.963**
	255	EM	32.75	5.76	0.961
		FOTV	33.06	6.07	0.970
		AEEPBD	**33.33**	**6.34**	**0.973**
Gaussian	3000	EM	38.42	7.17	0.971
		FOTV	38.84	7.59	0.980
		AEEPBD	**39.14**	**7.89**	**0.982**
	1000	EM	37.27	6.89	0.953
		FOTV	37.52	7.14	0.961
		AEEPBD	**37.80**	**7.42**	**0.964**
	255	EM	34.93	7.11	0.961
		FOTV	35.35	7.53	0.969
		AEEPBD	**35.60**	**7.78**	**0.970**

TABLE III Numerical results obtained via different models for "Brain" images under different types of blur and noise levels.

Blur	P	Model	PSNR	ISNR	SSIM
Motion	3000	EM	22.12	4.03	0.828
		FOTV	22.56	4.47	0.834
		AEEPBD	**22.92**	**4.83**	**0.838**
	1000	EM	21.89	3.84	0.842
		FOTV	22.31	4.25	0.847
		AEEPBD	**22.62**	**4.57**	**0.850**
	255	EM	21.57	3.68	0.869
		FOTV	21.92	4.03	0.871
		AEEPBD	**22.11**	**4.22**	**0.874**
Gaussian	3000	EM	23.64	5.38	0.836
		FOTV	24.15	5.89	0.840
		AEEPBD	**24.38**	**6.12**	**0.843**
	1000	EM	22.74	4.53	0.828
		FOTV	23.18	4.97	0.844
		AEEPBD	**23.34**	**5.13**	**0.845**
	255	EM	22.41	4.30	0.817
		FOTV	22.82	4.71	**0.838**
		AEEPBD	**22.96**	**4.85**	**0.838**

TABLE IV Numerical results gained through different models for "Triangle" images under different types of blur and noise levels.

Blur	P	Model	PSNR	ISNR	SSIM
Motion	3000	EM	36.46	14.47	0.978
		FOTV	36.87	14.88	0.990
		AEEPBD	**37.13**	**15.14**	**0.997**
	1000	EM	35.36	11.32	0.981
		FOTV	35.50	11.77	0.986
		AEEPBD	**35.75**	**12.02**	**0.989**
	255	EM	30.15	9.45	0.979
		FOTV	30.47	9.77	0.993
		AEEPBD	**30.68**	**9.98**	**0.995**
Gaussian	3000	EM	36.41	14.88	0.985
		FOTV	36.90	15.37	0.991
		AEEPBD	**37.15**	**15.62**	**0.994**
	1000	EM	33.05	13.24	0.979
		FOTV	35.02	13.59	0.982
		AEEPBD	**35.24**	**13.81**	**0.987**
	255	EM	32.29	11.31	0.971
		FOTV	32.72	11.74	**0.991**
		AEEPBD	**32.91**	**11.93**	**0.991**

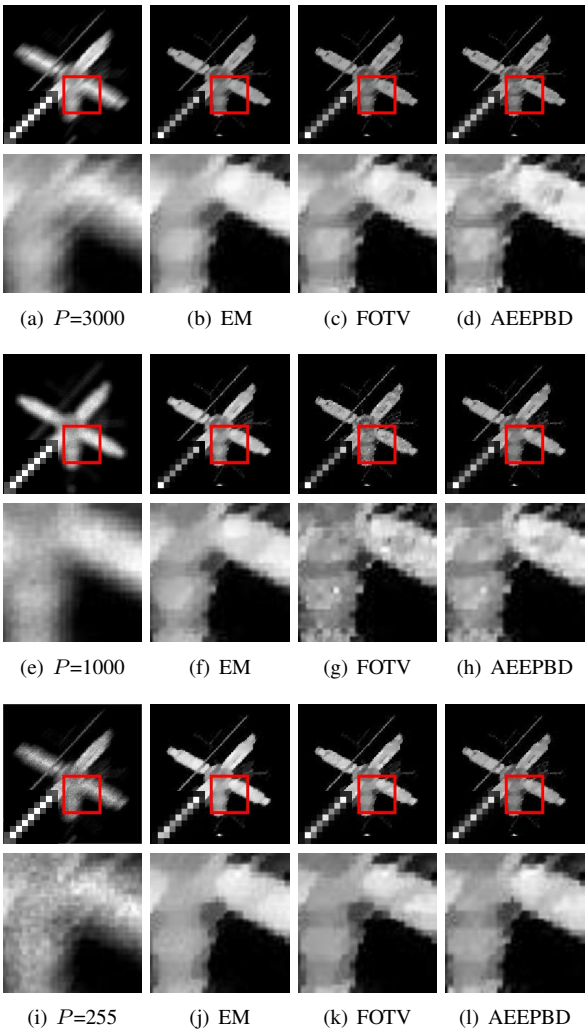

(a) P=3000 (b) EM (c) FOTV (d) AEEPBD

(e) P=1000 (f) EM (g) FOTV (h) AEEPBD

(i) P=255 (j) EM (k) FOTV (l) AEEPBD

Fig. 3. Blind restoration results obtained using different methods for "Satellite" images with linear motion blur at different peak values: P=3000 (rows 1, 2), P=1000 (rows 3, 4), and P=255 (rows 5, 6).

while the restoration result of the FOTV model exhibits noticeable staircase effects. However, due to the utilization of a high-order regularization in AEEPBD, the staircase effects are mitigated to some extent, while preserving a significant amount of image details. In Fig. 4, when the peak level is 255, it is evident that the blur kernel restored by AEEPBD is closer to the original blur kernel, and due to the presence of the adaptive weighted matrix, the local structure of the image is better preserved.

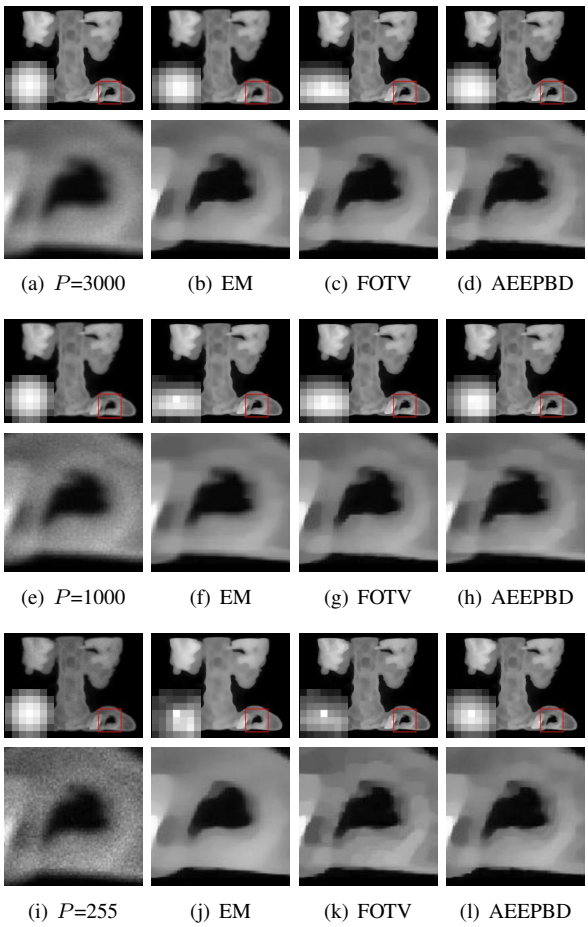

(a) P=3000 (b) EM (c) FOTV (d) AEEPBD

(e) P=1000 (f) EM (g) FOTV (h) AEEPBD

(i) P=255 (j) EM (k) FOTV (l) AEEPBD

Fig. 4. Blind restoration results acquired by different approaches for "Spine" images with Gaussian blur at different peak values: P=3000 (rows 1, 2), P=1000 (rows 3, 4), and P=255 (rows 5, 6).

Figs. 5 and 6 present the restored images, the residual images, and the recovered blur kernels for the synthetic images. Notably, the images recovered by AEEPBD appear smoother with sharper edges, offering significant advantages for PSF estimation. Contrastingly, we observe from the residual images that EM and FOTV struggle to recover most structural details, resulting in poor edge maintenance. AEEPBD manages to mitigate the staircase effects to some extent. This improvement is attributed to the adaptive weighted matrix employed by AEEPBD, which adjusts the direction of the gradient operator to tend toward larger weights, thereby enhancing the clarity of image local details. Additionally, the proposed method enhances the image contrast while removing noise, particularly noticeable in the "Brain" image. From the restored blur kernels, compared to EM and FOTV, the blur kernel restored by AEEPBD is closer to the original one.

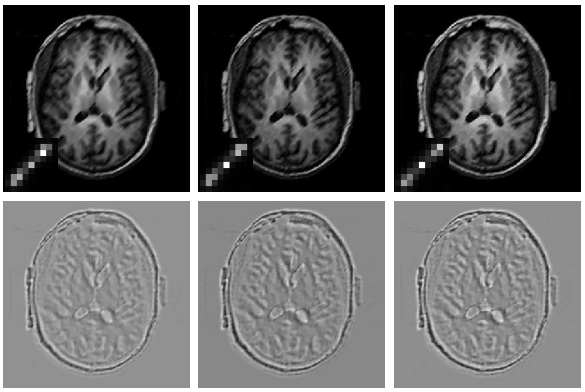

(a) EM (b) FOTV (c) AEEPBD

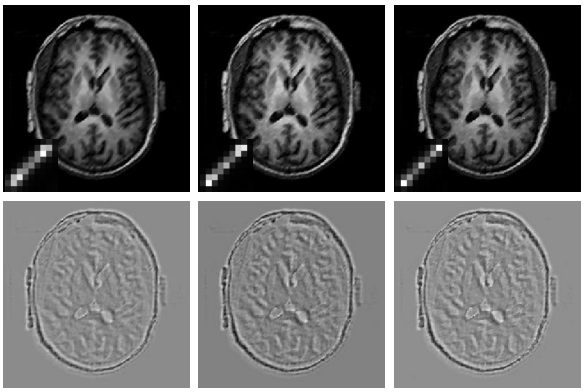

(d) EM (e) FOTV (f) AEEPBD

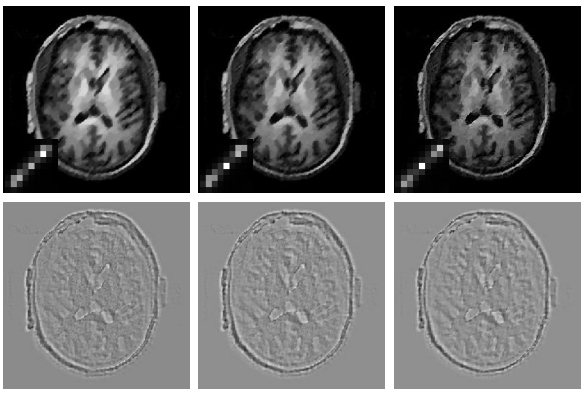

(g) EM (h) FOTV (i) AEEPBD

Fig. 5. Blind restoration results obtained by diverse methods for "Brain" images with linear motion blur at different peak values: P=3000 (rows 1, 2), P=1000 (rows 3, 4), and P=255 (rows 5, 6).

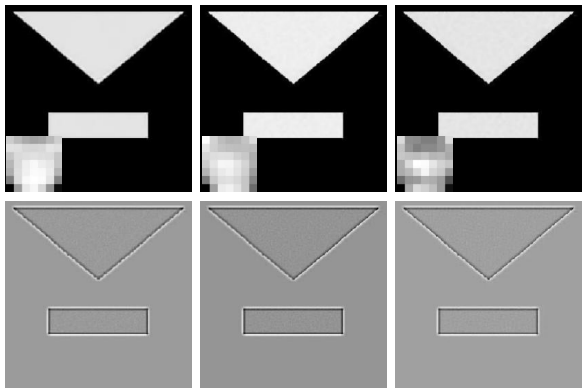

(a) EM (b) FOTV (c) AEEPBD

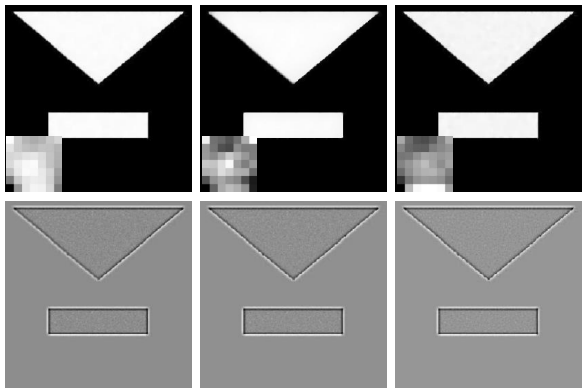

(d) EM (e) FOTV (f) AEEPBD

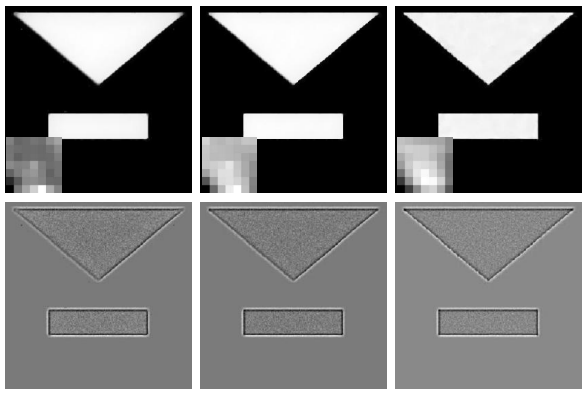

(g) EM (h) FOTV (i) AEEPBD

Fig. 6. Blind restoration results obtained by diverse approaches for "Triangle" images with Gaussian blur at different peak values: P=3000 (rows 1, 2), P=1000 (rows 3, 4), and P=255 (rows 5, 6).

V. CONCLUSION

In this paper, we proposed a novel blind restoration model for Poisson images based on the adaptive Euler's elastica regularization. Furthermore, we developed an efficient ADMM to solve it. Experimental results on both natural and synthetic images demonstrated that compared to other state-of-the-art methods, AEEPBD achieved better restoration effects, even in the presence of complex energy distributions in PSFs. In the future, we plan to explore acceleration techniques to further reduce computational costs. Additionally, we intend to extend the adaptive Euler's elastica regularization to other image processing challenges, such as image segmentation, hyperspectral image super-resolution, and hyperspectral image unmixing.

REFERENCES

[1] T. Rasal, T. Veerakumar, B. N. Subudhi, and S. Esakkirajan, "Fluorescence Microscopy Image Noise Reduction Using IEMD-based Adaptive Thresholding Approach," *Signal, Image and Video Processing*, vol. 17, no 1, pp. 237-245, 2023.

[2] V. Mannam, Y. Zhang, Y. Zhu, E. Nichols, Q. Wang, V. Sundaresan, S. Zhang, C. Smith, P. W. Bohn, and S. S. Howard, "Real-time Image Denoising of Mixed Poisson-Gaussian Noise in Fluorescence Microscopy Images using ImageJ," *Optica*, vol. 9, no. 4, pp. 335-345, 2022.

[3] G. J. Matheson, L. Ge, M. Zhang, B. Sun, Y. Tu, F. Zanderigo, A. F. Morèn, and R. T. Ogden, "Parametric and Non-parametric Poisson Regression for Modelling of the Arterial Input Function in Positron Emission Tomography," *EJNMMI Physics*, vol. 10, no. 1, p. 72, 2023.

[4] J. Sheng, P. Huang, R. Zhou, Z. Li, X. Yang, and J. Wang, "A Novel Reconstruction Method Combining Multi-detector SPECT with an Elliptical Orbit and Computer Tomography for Cardiac Imaging," *Scientific Reports*, vol. 13, no. 1, p. 15005, 2023.

[5] M. Diwakar, P. Kumar, P. Singh, A. Tripathi, and L. Singh, "An Efficient Reversible Data Hiding using SVD over a Novel Weighted Iterative Anisotropic Total Variation based Denoised Medical Images," *Biomedical Signal Processing and Control*, vol. 82, p. 104563, 2023.

[6] Z. F. Pang, Y. M. Zhou, T. Wu, and D. J. Li, "Image Denoising via a New Anisotropic Total-variation-based Model," *Signal Processing: Image Communication*, vol. 74, pp. 140-152, 2019.

[7] K. Jon, J. Liu, X. Lv, and W. Zhu, "Poisson Noisy Image Restoration via Overlapping Group Sparse and Nonconvex Second-order Total Variation Priors," *Plos One*, vol. 16, no. 4, p. e0250260, 2021.

[8] J. Xiang, H. Xiang, and L. Wang, "Poisson Noise Image Restoration Method based on Variational Regularization," *Signal, Image and Video Processing*, vol. 17, no. 4, pp. 1555-1562, 2023.

[9] D. D. Serafino, G. Landi, and M. Viola, "Directional TGV-based Image Restoration under Poisson Noise," *Journal of Imaging*, vol. 7, no. 6, pp. 99, 2021.

[10] X. C. Tai, J. Hahn, and G. J. Chung, "A Fast Algorithm for Euler's Elastica Model using Augmented Lagrangian Method," *SIAM Journal on Imaging Sciences*, vol. 4, no. 1, pp. 313-344, 2011.

[11] W. Tang, Z. Lin, and Y. Gong, "Gc-net: An Unsupervised Network for Gaussian Curvature Optimization on Images," *Journal of Signal Processing Systems*, vol. 95, no. 1, pp. 77-88, 2023.

[12] D. A. Fish, A. M. Brinicombe, E. R. Pike, and J. G. Walker, "Blind Deconvolution by Means of the Richardson–Lucy Algorithm," *JOSA A*, vol. 12, no. 1, pp. 58-65, 1995.

[13] Z. Xu, and E. Y. Lam, "Maximum a Posteriori Blind Image Deconvolution with Huber–Markov Random-field Regularization," *Optics Letters*, vol. 34, no. 9, pp. 1453-1455, 2009.

[14] H. Liu, Z. Zhang, S. Liu, T. Liu, L. Yan, and T. Zhang, "Richardson–Lucy Blind Deconvolution of Spectroscopic Data with Wavelet Regularization," *Applied Optics*, vol. 54, no. 7, pp. 1770-1775, 2015.

[15] H. Fang, L. Yan, H. Liu, and Y Chang, "Blind Poissonian Images Deconvolution with Framelet Regularization," *Optics Letters*, vol. 38, no. 4, pp. 389-391, 2013.

[16] W. Li, Q. Li, W. Gong, and S. Tang, "Total Variation Blind Deconvolution Employing Split Bregman Iteration," *Journal of Visual Communication and Image Representation*, vol. 23, no. 3, pp. 409-417, 2012.

[17] C. Xu, C. Zhang, M. Ma, and J. Zhang, "Blind Image Deconvolution via an Adaptive Weighted TV Regularization," *Journal of Intelligent and Fuzzy Systems*, vol. 44, no. 4, pp. 6497-6511, 2023.

[18] X. Gong, B. Lai, and Z. Xiang, "A L0 Sparse Analysis Prior for Blind Poissonian Image Deconvolution," *Optics Express*, vol. 22, no. 4, pp. 3860-3865, 2014.

[19] M. R. Chowdhury, J. Qin, and Y. Lou, "Non-blind and Blind Deconvolution under Poisson Noise using Fractional-order Total Variation," *Journal of Mathematical Imaging and Vision*, vol. 62, no. 9, pp. 1238-1255, 2020.

[20] W. Dong, S. Tao, G. Xu, and Y. Chen, "Blind Deconvolution for Poissonian Blurred Image with Total Variation and L0-norm Gradient Regularizations," *IEEE Transactions on Image Processing*, vol. 30, pp. 1030-1043, 2020.

[21] H. Liang, R. Liu, Z. Wang, J. Ma, and X. Tian, "Variational Bayesian Deep Network for Blind Poisson Denoising," *Pattern Recognition*, vol. 143, p. 109810, 2023.

[22] H. Liu, X. C. Tai, R. Kimmel, and R. Glowinski, "A Color Elastica Model for Vector-valued Image Regularization," *SIAM Journal on Imaging Sciences*, vol. 14, no. 2, pp. 717-748, 2021.

[23] X. Chen, X. Luo, G. Wangy, and Y. Zhengy, "Deep Elastica for Image Segmentation," *in 2021 IEEE 18th International Symposium on Biomedical Imaging (ISBI)*, 2021, pp. 706-710.

[24] Y. He, S. H. Kang, and H. Liu, "Curvature Regularized Surface Reconstruction from Point Clouds," *SIAM Journal on Imaging Sciences*, vol. 13, no. 4, pp. 1834-1859, 2020.

[25] J. Song, H. Pan, Y. Zhang, W. Lu, J. Ding, W. Wei, W. Liu, Z. Pan, and J. Duan, "Three-Dimensional Surface Reconstruction from Point Clouds using Euler's Elastica Regularization," *Applied Sciences*, vol. 13, no. 23, p. 12695, 2023.

[26] M. Ma, and J. Yang, "Poisson Image Restoration via an Adaptive Euler's Elastica Regularization," *Journal of Intelligent and Fuzzy Systems*, vol. 45, no. 2, pp. 2095-2110, 2023.

[27] J. Zhang, P. Li, J. Yang, M. Ma, and C. Deng, "Poisson Image Restoration Using a Novel Directional TVp Regularization," *Signal Processing*, vol. 193, p. 108407, 2022.

[28] X. Song, J. Zhang, J. Lu, and S. Rao, "Blind Image Deconvolution Based on Adaptive Euler's Elastica Regularization," *IAENG International Journal of Computer Science*, vol. 51, no. 1, pp. 32-38, 2024.

[29] J. Ahmad, I. Touqir, and A. M. Siddiqui, "Efficient Dark Channel Prior Based Blind Image De-blurring," *Radioengineering*, vol. 30, no. 2, p. 417, 2021.

[30] A. Sawatzky, C. Brune, T. Kösters, F. Wübbeling, and M. Burger, "EM-TV Methods for Inverse Problems with Poisson Noise," *Level Set and PDE Based Reconstruction Methods in Imaging*, Lecture Notes in Mathematics, vol. 2090, pp. 71-142, 2013.

[31] J. Yang, M. Ma, J. Zhang, and C. Wang, "Noise Removal Using an Adaptive Euler's Elastica-based Model," *The Visual Computer*, vol. 39, no. 11, pp. 5485-5496, 2023.